Earth and Planetary Science Letters 422 (2015) 194–205

Contents lists available at ScienceDirect

Earth and Planetary Science Letters

www.elsevier.com/locate/epsl

Tissintite, $(Ca, Na, \square)AlSi_2O_6$, a highly-defective, shock-induced, high-pressure clinopyroxene in the Tissint martian meteorite

Chi Ma [a,*], Oliver Tschauner [b], John R. Beckett [a], Yang Liu [c], George R. Rossman [a], Kirill Zhuravlev [d], Vitali Prakapenka [d], Przemyslaw Dera [e], Lawrence A. Taylor [f]

[a] Division of Geological and Planetary Sciences, California Institute of Technology, Pasadena, CA 91125, USA
[b] High Pressure Science and Engineering Center and Department of Geoscience, University of Nevada, Las Vegas, NV 89154, USA
[c] Jet Propulsion Laboratory, California Institute of Technology, Pasadena, CA 91109, USA
[d] GSECARS, University of Chicago, Argonne National Laboratory, Argonne, IL 60439, USA
[e] Hawai'i Institute of Geophysics and Planetology, School of Ocean and Earth Science and Technology, University of Hawai'i at Mānoa, Honolulu, HI 96822, USA
[f] Planetary Geosciences Institute, Department of Earth and Planetary Science, University of Tennessee, Knoxville, TN 37996, USA

ARTICLE INFO

Article history:
Received 13 June 2014
Received in revised form 30 March 2015
Accepted 31 March 2015
Available online 25 April 2015
Editor: J. Brodholt

Keywords:
tissintite
$(CaNa\square)AlSi_2O_6$
new high-pressure pyroxene
Ca-Eskola
Tissint martian shergottite
synchrotron diffraction

ABSTRACT

Tissintite is a new vacancy-rich, high-pressure clinopyroxene, with a composition essentially equivalent to plagioclase. It was discovered in maskelynite (shocked plagioclase) and is commonly observed included within, or in contact with, shock-melt pockets in the Tissint meteorite, a depleted olivine-phyric shergottite fall from Mars. The simple composition of tissintite (An58–69) and its precursor plagioclase (An59–69) together with the limited occurrence, both spatially (only in maskelynite less than ~25 μm of a shock melt pocket) and in terms of bulk composition, make tissintite a "goldilocks" phase. It formed during a shock event severe enough to allow nucleation and growth of vacancy-rich clinopyroxene from a melt of not too calcic and not too sodic plagioclase composition that was neither too hot nor too cold. With experimental calibration, these limitations on occurrence can be used to place strong constraints on the thermal history of a shock event. The kinetics for nucleation and growth of tissintite are probably slower for more-sodic plagioclase precursors, so tissintite is most likely to occur in depleted olivine-phyric shergottites like Tissint and other highly shocked meteorites and lunar and terrestrial rocks that consistently contained calcic plagioclase precursors in the appropriate compositional range for a shock of given intensity.

Tissintite, $(Ca_{0.45}Na_{0.31}\square_{0.24})(Al_{0.97}Fe_{0.03}Mg_{0.01})(Si_{1.80}Al_{0.20})O_6$, is a $C2/c$ clinopyroxene, containing 42–60 mol% of the Ca-Eskola component, by far the highest known. The cell parameters are $a = 9.21$ (17) Å, $b = 9.09$ (4) Å, $c = 5.20$ (2) Å, $\beta = 109.6$ (9)°, $V = 410$ (8) Å^3, $Z = 4$. The density is 3.32 g/cm^3 and we estimate a cell volume for the Ca-Eskola end-member pyroxene of 411 ± 13 Å^3, which is consistent with a previous estimate and, therefore, supports the importance of this component in clinopyroxenes from ultra-high pressure metamorphic rocks from the Earth's upper mantle. At least in $C2/c$ clinopyroxenes as sodic as tissintite, the a- and b-cell parameters as a function of vacancy concentration intersect at ~0.3 vacancies *pfu*, much lower than the Ca-Eskola end-member (0.5), an inversion of anisotropy suggesting an elastic instability that drives clinopyroxene toward a disordered trigonal structure closely related to that of wadeite; it may mark the boundary beyond which the breakdown of vacancy-rich clinopyroxene to a wadeite-structured phase + stishovite becomes stable, although this was not observed in Tissint.

1. Introduction

Because much of the Earth's interior lies hidden from view, we are left to infer its physical conditions, mineralogy, and bulk compositions through interpretation of seismic events, experiments on analog materials, theoretical modeling, examination of natural materials that sampled these regions, and by characterizing natural materials subjected to unusual processes. All of these venues can lead to a better understanding of the nature of planetary interiors (e.g., Akaogi, 2007; Ahrens et al., 2009; Stixrude and Lithgow-Bertelloni, 2012; Hirose et al., 2014; Litvin et al., 2014). Minerals produced in shock events can be particularly useful, be-

* Corresponding author.
E-mail address: chi@gps.caltech.edu (Chi Ma).

http://dx.doi.org/10.1016/j.epsl.2015.03.057
0012-821X/

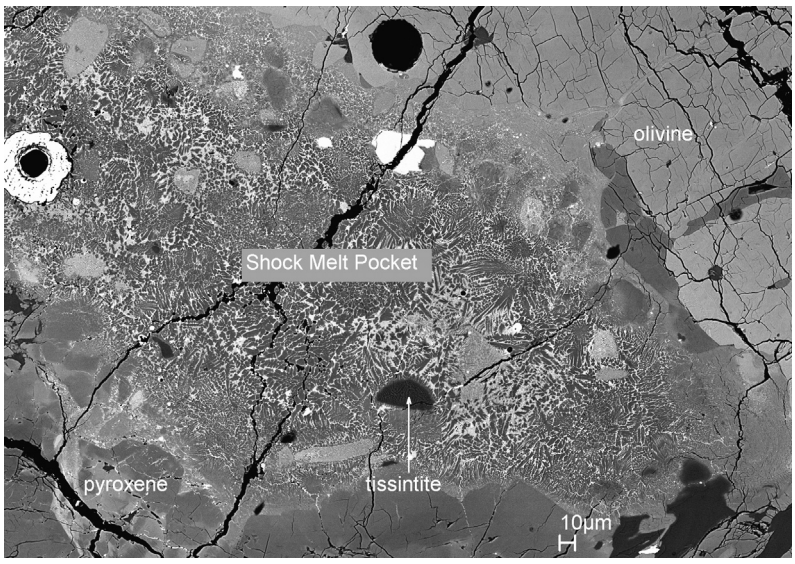

(a)

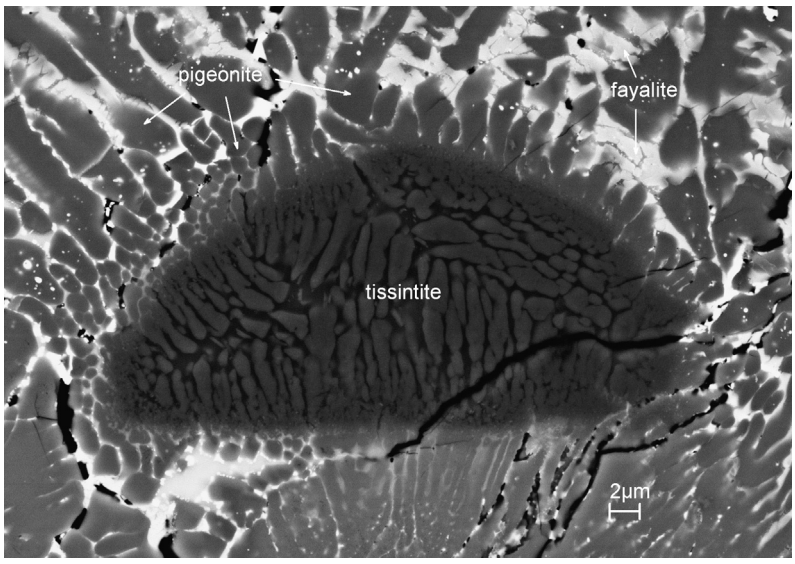

(b)

Fig. 1. (a) SEM BSE image showing tissintite in a shock melt pocket, in Tissint section UT2. (b) Enlarged BSE image revealing fine-grained tissintite with surrounding pigeonite and fayalite. (c–d) SEM BSE images of additional tissintite occurrences from UT1.

cause of their potential for constraining the severity of the shock and, more generally, the properties of phases at high pressures and temperatures (e.g., Stöffler et al., 1991; Ohtani et al., 2004; Sharp and DeCarli, 2006; Walton et al., 2014). In this study, we describe a new mineral, "tissintite," with a shock-induced clinopyroxene structure that has a plagioclase equivalent composition, $(Ca, Na, \square)AlSi_2O_6$, requiring an extraordinarily large concentration of vacancies, roughly one quarter of the M2 sites. It is potentially an important indicator of the shock-metamorphic processes that launched martian meteorites and other highly shocked rocks, and its existence provides a basic ground truth for building thermodynamic models of vacancy-rich clinopyroxenes in ultra-high pressure metamorphic rocks.

Tissintite was discovered in and is named after the martian meteorite Tissint, which fell near Tissint, Morocco on 18 July 2011. Tissint is a fresh, olivine-phyric shergottite with strong-shock features and has been subjected to intense study since its fall (e.g., Aoudjehane et al., 2012; Baziotis et al., 2013; Herd et al., 2013; Udry et al., 2013; Walton et al., 2014). The mineral and its name (tissintite) were approved by the Commission on New Minerals, Nomenclature and Classification (CNMNC) of the International Mineralogical Association (IMA 2013-027) (Ma et al., 2013a). Ma et al. (2014) give a preliminary report of the results of this study.

2. Sample and analytical methods

2.1. Type material

Tissintite was identified in sections UT1, UT2 and UT3 (e.g., Figs. 1–2; formerly referred to as MT-1, 2, 3 by Baziotis et al., 2013) prepared at the University of Tennessee from a Tissint fragment with a partial fusion crust. Type material in all three sections was deposited in the Meteorite Collection of the Frank H. McClung Museum at the University of Tennessee, Knoxville, TN 37996, USA. Based on the common occurrence of tissintite in each of these sections, tissintite is likely to occur in most samples of the Tissint meteorite.

2.2. Analytical methods

Electron probe microanalysis (EPMA), high-resolution scanning electron microscopy (SEM), electron back-scatter diffraction

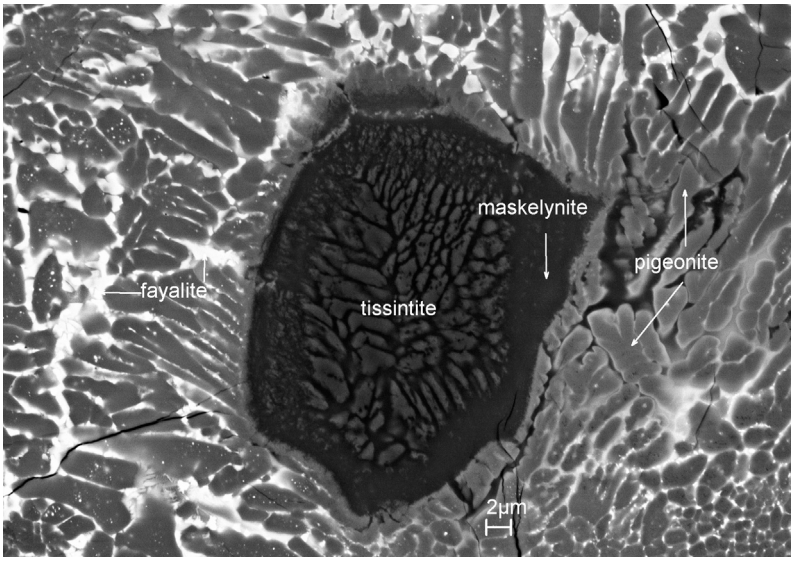

(c)

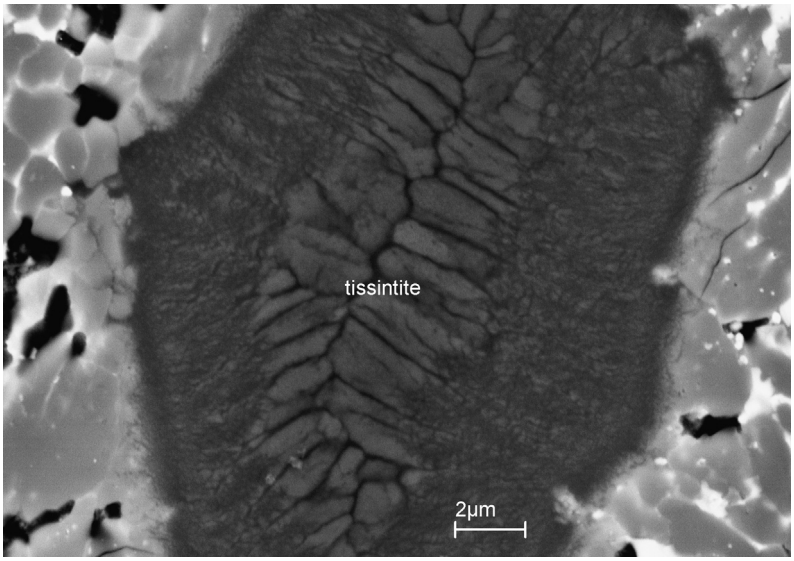

(d)

Fig. 1. (*continued*)

(EBSD), synchrotron X-ray diffraction, and micro-Raman analyses were used to determine the composition of tissintite, its physical properties and structure, and to characterize associated phases. Back-scatter electron (BSE) imaging was performed using a ZEISS 1550VP field emission SEM. The EBSD analyses were performed using an HKL EBSD system on the ZEISS 1550VP SEM, operated at 20 kV and 6 nA in focused-beam mode with a 70° tilted stage and variable pressure mode (15 Pa). Chemical analyses of tissintite and associated minerals were determined using a JEOL 8200 electron microprobe (WDS: 15 kV; 5 nA; beam in focused mode) interfaced with the Probe for EPMA program from Probe Software, Inc. Standards for analysis were anorthite (Si$K\alpha$, Al$K\alpha$, Ca$K\alpha$); albite (Na$K\alpha$); fayalite (Fe$K\alpha$); forsterite (Mg$K\alpha$); Mn_2SiO_4 (Mn$K\alpha$); TiO_2 (Ti$K\alpha$); Cr_2O_3 (Cr$K\alpha$); and microcline (K$K\alpha$). Quantitative elemental microanalyses were processed with the CITZAF correction procedure (Armstrong, 1995), and analytical results are given in Table 1.

Diffraction data were collected at the undulator beamline 13-IDD (GSECARS, APS, Argonne National Laboratory) and at the superconducting, bending-magnet beamline 12.2.2, (ALS, Lawrence Berkeley National Laboratory), using a primary beam energy of 37 keV (0.3344 Å) and 30 keV (0.4133 Å). The uncoated thin section UT2 was examined with no additional preparation. At the 13-IDD location, single-crystal diffraction data of tissintite crystallites were collected with an X-ray beam focused to $\sim 3 \times 4$ μm^2 by vertical and horizontal Kirkpatrick–Baez mirrors. A MAR165 CCD detector was used for collecting image frames in forward geometry, using 0.5° increments for the phi axis, while chi and theta angles of reflections were internal detector coordinates. The GSE_ADA software package (Dera et al., 2013) was used for data collection, peak-search, peak-fitting, correction of polarization, and for peak-integration. The RSV (Dera et al., 2013) was used for indexing and to export of hkl-files. A complementary set of diffraction data was collected at beamline ALS 12.2.2, with a beam size of 15×20 μm^2, in order to acquire a powder-like diffraction pattern for tissintite.

Raman spectroscopic microanalysis was conducted using a 514.3 nm solid-state laser in a Renishaw M1000 micro-Raman spectrometer system on type tissintite in section UT2, using methods described in Ma and Rossman (2008, 2009). The spot size was ~2 μm.

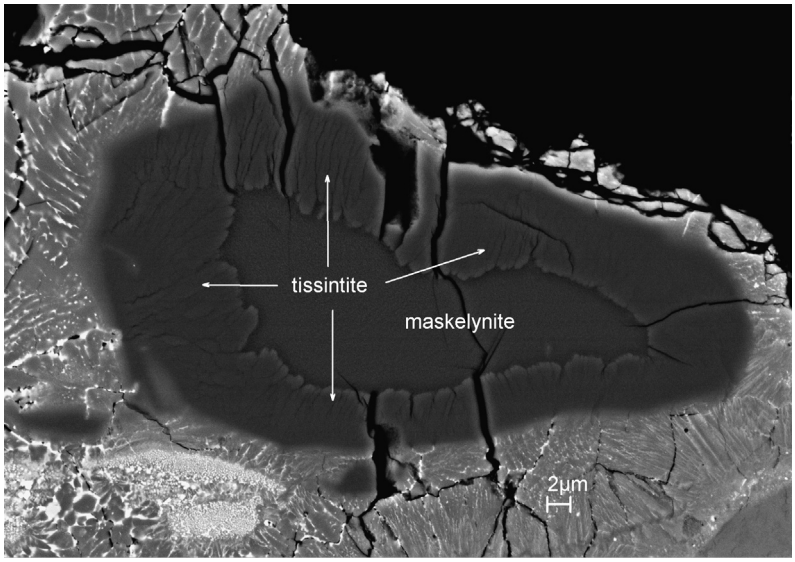

(a)

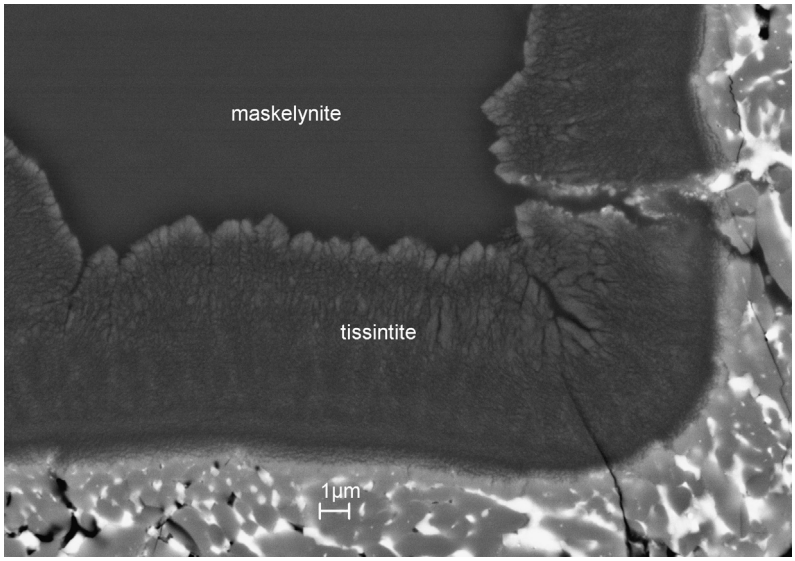

(b)

Fig. 2. SEM BSE images showing tissintite crystals in Tissint section UT1. (a) Tissintite forms a rim that completely surrounds plagioclase glass in the interior and thereby separates it from the host melt pocket. (b) A close-up of a rim region from a different tissintite occurrence in UT1, showing individual crystals. The crystal size is generally in the range of 100–500 nm; crystals elsewhere in the meteorite can be as long as ~4 μm. (c) Tissintite crystals rim a large maskelynite where it came into contact with an adjacent melt pocket. The tissintite rim extends ~25 μm away from portions of the maskelynite that was in direct with the quench mat of the melt pocket in the plane of the section. The maskelynite containing the tissintite extends ~150 μm away from the melt pocket, but only within the closest ~25 μm does tissintite occur. Ringwoodite and the new mineral ahrensite occur on the opposite side of this melt pocket, ~150 μm away from the tissintite.

3. Results

3.1. Occurrence, appearance, physical and optical properties

The Tissint "rock" contains mostly zoned olivine and pyroxene (mainly pigeonite), with minor chromite and ilmenite, plus shock-melt pockets. An assortment of previously reported shock-related phases includes ahrensite, akimotoite, diamond, jadeite, linguite, majorite, maskelynite, ringwoodite, stishovite, tuite, and xieite (Baziotis et al., 2013; El Goresy et al., 2013a, 2013b; Kuchka et al., 2013; Ma et al., 2014; Walton et al., 2014). The new high-pressure mineral, ahrensite (Fe analog of ringwoodite, γ-$(Fe,Mg)_2SiO_4$, IMA 2013-028) (Ma et al., 2013b) occurs after olivine in ferroan rims on olivine phenocrysts, where the rim is in contact with a melt pocket.

Tissintite occurs in two basic textural forms, both consisting of fine-grained aggregates in maskelynite. The aggregates are composed of elongate to irregularly shaped single crystals, ranging from 100 nm in diameter up to $2 \times 2 \times 4$ μm^3 in size, with aspect ratios in the plane of the section of ~1 to ~10 and with no coexisting crystalline phases. In the first textural style (Fig. 1), crystals form wormy intergrowths within a matrix of maskelynite and cellular tissintite. This tissintite–glass assemblage is completely enclosed by the host melt pocket, which quenched to mixture of pigeonite and fayalite. In a second textural type (Fig. 2), the precursor maskelynite is in contact with, but may not be completely enclosed by the melt pocket. Here, tissintite forms rims separating maskelynite from the contacting shock-melt pocket. There may be additional aggregates of tissintite forming inclusions within the glass (Fig. 2c). Note in Fig. 2c (also true of other occurrences) that maskelynite more than ~25 μm from the shock-melt pocket shows no tissintite; this is a conservative upper-limit distance because shock-melt closest to a tissintite aggregate may well have been out of the plane of the thin sec-

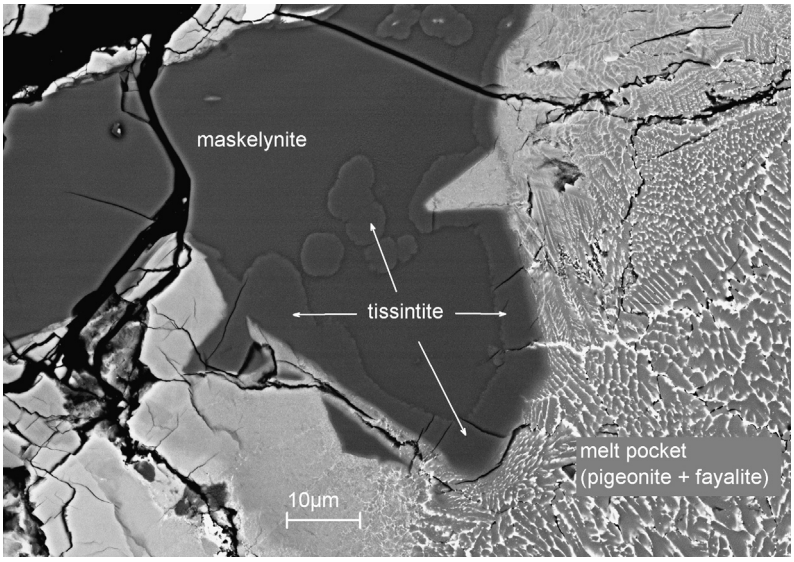

(c)

Fig. 2. (*continued*)

Table 1
Electron microprobe analytical results for wormy and rimming tissintite, and associated phases.

Oxide	Wormy type tissintite	Maskelynite associated with wormy tissintite	Rimming tissintite	Maskelynite associated with rimming tissintite	Maskelynite away from melt pockets	Pigeonite surrounding tissintite	Fayalite[d] surrounding tissintite
	$n = 6$[a]	$n = 6$	$n = 6$	$n = 9$	$n = 17$	$n = 7$	$n = 5$
SiO_2	53.0(0.3)[b]	52.8(0.9)	53.2(0.3)	52.6(0.3)	53.7(0.9)	53.6(0.8)	35(1)
TiO_2	0.08(0.03)	0.07(0.04)	0.05(0.02)	0.04(0.02)	0.07(0.03)	0.09(0.04)	0.56(0.09)
Al_2O_3	29.2(0.3)	28.5(0.5)	29.7(0.2)	29.3(0.2)	29.1(0.6)	2.7(0.5)	3.3(0.5)
FeO	0.96(0.02)	1.3(0.4)	0.85(0.06)	0.79(0.07)	0.7(0.1)	13.3(0.7)	40(1)
MgO	0.18(0.02)	0.3(0.3)	0.17(0.02)	0.17(0.04)	0.15(0.06)	22.6(0.6)	15(1)
CaO	12.5(0.2)	12.4(0.1)	13.0(0.2)	12.9(0.1)	12.5(0.7)	6.1(0.5)	4.7(0.5)
Na_2O	4.7(0.2)	3.53(0.08)	3.9(0.1)	3.5(0.1)	3.9(0.3)	0.4(0.1)	0.39(0.05)
K_2O	0.06(0.01)	0.08(0.03)	0.06(0.01)	0.10(0.03)	0.1(0.1)	b.d.	0.06(0.03)
Cr_2O_3	b.d.[c]	b.d.	b.d.	b.d.	b.d.	0.52(0.08)	0.56(0.06)
MnO	b.d.	b.d.	b.d.	b.d.	b.d.	0.46(0.07)	0.85(0.03)
Total	100.7	99.0	100.9	99.4	100.2	99.8	100
Ca/(Ca + Na + K) atomic ratio as %	59	66	65	67	63		
No. O atoms	6	8	6	8	8	6	4
Si	1.80	2.42	1.80	2.40	2.43	1.95	1.01
Ti	0.00	0.00	0.00	0.00	0.00	0.00	0.01
Al	1.17	1.54	1.18	1.58	1.55	0.12	0.11
Fe	0.03	0.05	0.02	0.03	0.03	0.41	0.96
Mg	0.01	0.02	0.01	0.01	0.01	1.23	0.64
Ca	0.45	0.61	0.47	0.63	0.61	0.24	0.14
Na	0.31	0.31	0.26	0.31	0.34	0.03	0.02
K	0.00	0.00	0.00	0.01	0.01		0.00
Cr						0.01	0.01
Mn						0.01	0.02
Sum cations	3.77	4.95	3.74	4.97	4.98	4.00	2.92

[a] n = number of analyses.
[b] Errors given inside parentheses are one standard deviation of the mean based on all of the analyses.
[c] b.d. = below detection limit: 0.02 wt% K, 0.05 wt% Cr, 0.06 wt% Mn.
[d] Slightly contaminated by co-existing pigeonite.

tion. Tissintite is not observed at every maskelynite-shock pocket contact and, since compositions of tissintite-free and tissintite-bearing maskelynites are comparable, this suggests nucleation effects driven by differences in local thermal histories (e.g., larger melt pockets stay hot longer than small ones). For reasons of simplicity, we use the term 'maskelynite' in this paper for any non-crystalline material with feldspar composition and with no distinction as to whether the material is quenched melt or diaplectic glass.

3.2. Chemical composition and crystallography

The compositions of tissintite and associated maskelynite are given in Table 1. The type tissintite has an empirical formula [based on 6 oxygen atoms per formula unit (*pfu*)] of $(Ca_{0.45}Na_{0.31}\square_{0.24})(Al_{0.97}Fe_{0.03}Mg_{0.01})(Si_{1.80}Al_{0.20})O_6$, leading to a general formula of $(Ca, Na, \square)Al(Si, Al)_2O_6$. Compositions of tissintites observed in this study are fairly close to $(Ca_{1/2}Na_{1/4}\square_{1/4})(Al)(Al_{1/4}Si_{7/4})O_6$ with Ca#s [$100 * Ca/(Ca + Na)$

on a molar basis] ranging from 58 to 69, and vacancy concentrations based on the stoichiometry, from 0.21–0.30 sites *pfu*. Compositions are consistent with vacancies being restricted to the M2 site with nearly full occupancy of M1 by Al. Tissintite compositions are quite close to those of plagioclase. For the same composition, we can describe the connection between the two as

$$\frac{3}{4}(Ca_xNa_{1-x})(Al_{1+x}Si_{3-x})O_{8(\text{plagioclase})}$$
$$= (Ca_{3x/4}Na_{(1-x)/4}\square_{1/4})(Al)(Al_{(3x-1)/4}Si_{3(3-x)/4})O_{6(\text{clinopyroxene})}.$$

This relation holds for $1 \geq x \geq 1/3$ (i.e., for An33.3–An100). For $x < 1/3$, negative amounts of tetrahedral Al are required. For tissintite restricted to the equivalent albite–anorthite join, a likely Na-free end-member is $(Ca_{3/4}\square_{1/4})Al(Si_{1.5}Al_{0.5})O_6$, where 1/4 of the M2 sites are vacant. The Ca-Eskola molecule, $(Ca_{1/2}\square_{1/2})AlSi_2O_6$, is a possible Ca-endmember for tissintite, where half of the M1 sites are vacant.

Synchrotron diffraction was used to constrain the crystallographic properties of tissintite. The observed reflections arose from a mixture of phases, primarily fayalite and pigeonite from nearby quenched shock melt, and tissintite. We first indexed the reflections of coexisting fayalite crystals. Of the remaining reflections, as listed in Table 2, 24 were found to belong to one crystallite of monoclinic symmetry with cell dimensions of $a = 9.2$ (2) Å; $b = 9.09$ (4) Å; $c = 5.20$ (2) Å; and $\beta = 109.6$ (9) Å, where one-sigma errors are given inside parentheses. This unit cell, in combination with the assignment of space group $C2/c$, matches the EBSD pattern of tissintite with a mean angular deviation $< 0.34°$. In contrast, the space groups $P2_1/c$ (pigeonite) or $P2/n$ (ordered omphacite) cannot fit the EBSD pattern. Walton et al. (2014) report "tissintite" with a $P2_1/c$ structure based on SAED patterns obtained using transmission electron microscopy. The different space group (i.e., $P2_1/c$ rather than $C2/c$) either implies a new tissintite-like mineral, which could then yield an additional statement of formation conditions, or contamination of the analyzed volume of $C2/c$ tissintite by adjacent $P2_1/c$ pigeonite, as was observed in synchrotron diffraction data described below.

The number of unique reflections belonging to this and other individual crystallites of tissintite was too small for structure analysis. Moreover, some of the observed intensities appear to be affected by extinction from major reflections of coexisting phases in the examined sample (i.e., fayalite and pigeonite). We can nevertheless compute the density of tissintite as 3.32 g/cm^3 from these cell parameters and the composition.

Micro-synchrotron X-ray diffraction patterns of multicrystal-multiphase aggregates frequently suffer from extinction by coexisting phases; this effect can be compensated for by large statistics of reflections, but these are not available for tissintite. Therefore, we collected a complementary set of synchrotron diffraction data at beamline ALS 12.2.2, with a beam area of 15×20 μm^2, and the intent of acquiring a powder-like diffraction pattern for tissintite. However, this dataset also evades a fully quantitative interpretation because of the prominent texture of the tissintite aggregates (e.g., Figs. 1–2) and the super-imposition of reflections from an array of adjacent pigeonite crystallites, which cannot be well accounted for by Rietveld refinement or masking (Hammersley et al., 1996). Although the different weight of overlapping reflections in textures of polycrystals can be assessed, the overlap of the pattern of tissintite with sporadic single-crystal reflections of adjacent pigeonite limited the possibility of fitting the aggregate texture.

Absent a more comprehensive dataset for tissintite, the internal structural parameters, such as the vacancy distribution between M1 and M2, cannot be fully assessed because they correlate to a large extent with crystallite orientations. We optimized for this textural effect by using spherical harmonics (Von Dreele, 1997) for the two extreme cases of all vacancies on M2 (Ca-Eskola molecule) and all vacancies on M1. The Rietveld refinements slightly favor the Ca-Eskola molecule, with an Rwp (Rietveld weighted profile factor) of 9.0% over a model with vacancies relegated to the M1 site, which yields an Rwp of 10.5%. We note that a structure model with ~50–60% Ca-Eskola molecule in tissintite is clearly supported by the cell parameters and volume as shown in the Supplement. Reflections attributable to stishovite were not observed.

Table 2
Observed reflections of tissintite.

h	*k*	*l*	d (Å)
−3	3	3	1.49261
−2	2	2	2.13817
−2	6	0	1.41584
−2	8	2	1.04032
−1	−1	3	1.69708
−1	1	2	2.56655
−1	3	0	2.92434
−1	5	−1	1.67728
−1	5	1	1.69769
−1	7	0	1.27315
0	−2	2	2.13957
0	4	−2	1.67252
1	−3	0	2.88943
2	−6	0	1.44849
2	−6	3	1.01711
2	−4	−2	1.67187
2	−4	1	1.76702
2	−2	−2	2.22146
2	−2	−1	2.99316
3	−5	−1	1.53530
3	−5	1	1.38139
3	−1	−3	1.65521
4	−2	−3	1.49224
4	0	−5	1.02196

The Raman spectrum of type tissintite, shown in Fig. 3, is similar to that of jadeite with major features at 203; 377; 415; 523; 572; 693; and 1000 cm^{-1}. These features are consistent with both experimental and theoretical expectations for a $C2/c$ clinopyroxene (e.g., Yang et al., 2009; Prencipe, 2012), but noticeably broader than is typical of clinopyroxene reference phases. For example, the full-width at half-height of the 693 cm^{-1} tissintite band is about 25 cm^{-1} compared to the corresponding jadeite band at 700 cm^{-1} that is 9 cm^{-1} wide. In the jadeite spectrum, there is a pair of sharply defined bands near 1000 cm^{-1}. In tissintite, there is a single broad band of about 83 cm^{-1} width. These anomalous widths are indicative of cation disorder in the tissintite structure (e.g., Ca–Na on the M2 site). As Fig. 3 indicates, the Raman spectrum of tissintite is inconsistent with either maskelynite or plagioclase.

4. Discussion

Tissintite is a clinopyroxene, $(Ca, Na, \square)AlSi_2O_6$, in which the M1 site is completely (or almost so) occupied by Al. It can be thought of as the Ca-analog of jadeite with ~1/4 of the M2 sites being vacant, with a likely Ca-end member of $(Ca_{3/4}\square_{1/4})Al(Si_{3/2}Al_{1/2})O_6$ for an anorthite-equivalent composition, or with greater vacancy concentrations, a Ca-Eskola component (Ca-Es: $(Ca_{1/2}\square_{1/2})AlSi_2O_6$). The connection between tissintite with a Ca# of 2/3 and other pyroxene components can be considered as:

$$(Ca_{1/2}Na_{1/4}\square_{1/4})Al_{5/4}Si_{7/4}O_6$$
$$= 1/2\,(Ca_{1/2}\square_{1/2})AlSi_2O_6 + 1/4\,NaAlSi_2O_6 + 1/4\,CaAl_2SiO_6$$

or

$$\text{tissintite} = 1/2\,\text{Ca-Eskola} + 1/4\,\text{jadeite} + 1/4\,\text{kushiroite}.$$

Tissintite is quite aluminous (~30 wt% Al_2O_3), but kushiroites are more so (up to 46 wt%; Kimura et al., 2009; Ma et al., 2009), and

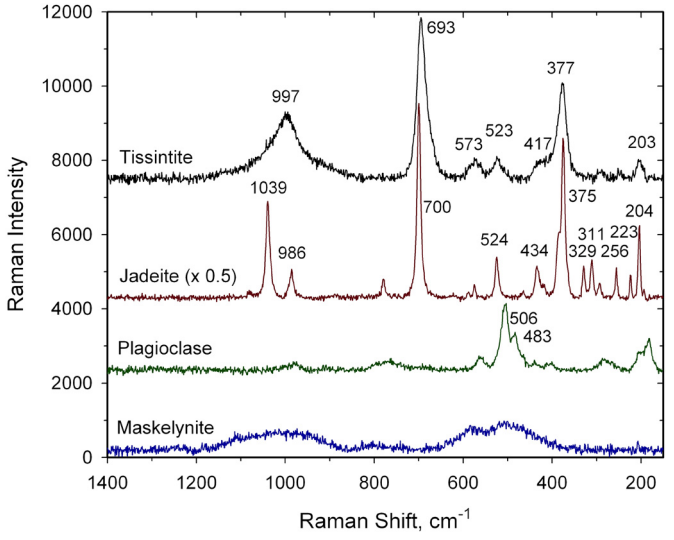

Fig. 3. Raman spectra of tissintite shown in Fig. 1b, maskelynite in Tissint (UT2), jadeite from a polished slab of colorless, polycrystalline Burmese jadeite, and plagioclase (An69.4) from the Ponderosa Mine, Harney Co., OR, USA (Johnston et al., 1991).

it is the extraordinarily high vacancy concentration on the M2 site that is the salient structural characteristic. In the sections we studied, 21 to 30% of the M2 sites are vacant, making tissintite the most highly defective natural clinopyroxene reported to date. Tissintite also exhibits more vacancies than any synthetic clinopyroxene, of which we are aware. Zhao et al. (2011) reported synthesizing aluminous clinopyroxenes with up to ~20% vacancies on M2, but <10% is more typical of clinopyroxenes in experimental run products with mantle phase assemblages (e.g., Irifune et al., 1986; Konzett et al., 2008; Pertermann and Hirschmann, 2002). If vacancies on M2 are accounted for through the Ca-Eskola component, as is typical for work on ultra-high pressure metamorphism and the petrology of the upper mantle, then tissintites have 42–60% Ca-Eskola component. This is up to 50% more than concentrations in the most vacancy-rich synthetic clinopyroxene and several times observed values in other natural clinopyroxenes (e.g., Oberti and Caporuscio, 1991; Smyth, 1980). It has been argued that substantially higher vacancy concentrations were achieved in symplectites from ultra-high-pressure metamorphic rocks, but if so, they shed vacancies during decompression, perhaps through the commonly observed exsolution of silica (e.g., Katayama et al., 2000). The discovery of tissintite makes the existence of these postulated vacancy-rich clinopyroxenes more plausible but knowledge of the thermodynamic properties is necessary for a quantitative assessment and this is not currently available. The existence of tissintite does make it likely that vacancy-rich clinopyroxenes can be studied experimentally through synthesis on suitable bulk compositions at high pressures (i.e., calcic plagioclase ± additional silica).

Although errors on the measured cell parameters of tissintite are large, the values are consistent with expectations for a vacancy-rich $C2/c$ clinopyroxene, as shown in Fig. 4. Cell parameters and volumes of $C2/c$ clinopyroxenes are a strong function of Ca# (e.g., Wood et al., 1980), and since Ca# = 59 for the type tissintite, we show cell parameters and volumes for tissintite in Fig. 4 along with those of natural $C2/c$ clinopyroxenes with 54 < Ca# < 64 from McCormick (1986), Oberti and Caporuscio (1991), and Nestola et al. (2007), as a function of vacancy concentration on the M2 site. We used data from these sources rather than computing deviations of cation sums from 4 *pfu* because the structure analyses provide a more direct measurement of vacancy concentrations. Fig. 4a shows linear correlations between vacancy concentrations and axis lengths, although there is a hint of nonlinearity for *b*. The correlation between volume and vacancy concentration (Fig. 4c) is also linear within the scatter of data. The data for β at very low vacancy concentrations (Fig. 4b) indicate that β decreases with increasing concentration of vacancies; but, this negative slope must reverse at higher concentrations to be consistent with β in tissintite. In the Supplement, we estimate the cell volume of the Ca-Eskola molecule as 411 ± 13 Å^3 for the Ca-Eskola end-member using these data, which is potentially larger than but, within error, consistent with McCormick's (1986) assessment of 402 ± 5 Å^3.

An important feature of the trends shown in Figs. 4a–c is that the a- and b-axes intersect at a vacancy concentration of ~0.3 *pfu* and an axis length of ~9.15 Å, keeping in mind that the large error in the a-axis length of tissintite makes the precise location of the intersection rather uncertain. This 'inversion' of unit-cell anisotropy does not require, but is often associated with, a structural instability, so we examine whether or not a convergence of the *a*- and *b*-axis lengths can induce an instability in vacancy-rich clinopyroxenes. A first observation is that equality of the *a*- and *b*-axes in tissintite makes the unit cell equivalent to a *C*-centered orthorhombic cell, which in turn can be interpreted as a subgroup of a trigonal cell. An equivalent structure is obtained by a direct group–subgroup relationship between $C2/c$ and $P\bar{3}1c$ with transformation matrix (0 0 1|−1/2 1/2 0| 0 0 1), which maintains the axis lengths of the monoclinic cell but increases the angle from ~110 to 120°. The trigonal structure has higher multiplicities for all atoms and, therefore, the atoms are disordered on these high symmetry sites with partial occupancies. This is a purely geometric mapping, but two points are noteworthy:

1) The trigonal structure is related to the clinopyroxene structure through condensation *only* of zone center modes (Table 3). This means the transition can occur spontaneously without diffusion, and it can be of second order if the monoclinic angle approaches 120° at elevated temperature.
2) The trigonal structure has a marked resemblance to the structure of the wadeite–benitoite group and, in particular, to the known high-pressure decomposition product of feldspars $(K,Na)_2AlSi_2O_9$ (e.g., Kinomura et al., 1975; Yagi et al., 1994). It is plausible that a disordered trigonal structure is transient to decomposition of the vacancy-rich pyroxene to a wadeite-type silicate plus a high pressure silica polymorph. Unlike the monoclinic-trigonal transition described above, however, this process involves the diffusion of atoms.

These two points taken together suggest that there is an upper limit to the Ca-Eskola component in clinopyroxenes. For a Ca# ~60, this limit is ~0.3 M2 vacancies *pfu*. The most vacancy-rich of the tissintites in Tissint, which are the most vacancy-rich clinopyroxenes currently known, are close to this limiting concentration, but experimentation on bulk compositions off the albite–anorthite join would probably be required to test the proposed limit. The corresponding vacancy limit for Ca# = 100 (i.e., for the Ca-Eskola end member) is unknown, but it is possible that the Ca-Eskola molecule is not a physically attainable phase.

In addition to structural constraints limiting concentrations of vacancies on the M2 site in clinopyroxene, there are charge-balance restrictions. In Fig. 5, we show Ca# [molar Ca/(Ca + Na)] as a function of vacancy concentration on the M2 site. In this plot, we assign monovalent cations to M2 and assume that all vacancies are also on this site, with all other defects being present in negligible amounts. If the M1 site is then occupied only by trivalent and divalent cations (i.e., ignoring Ti), the maximum concentration of vacancies at any given Ca# is defined by an M1 site fully occupied by trivalent cations and tetrahedral sites fully occupied by Si. This leads to a curve defining a charge balance limit for M2 vacancies that extends from the origin (end-member jadeite) to

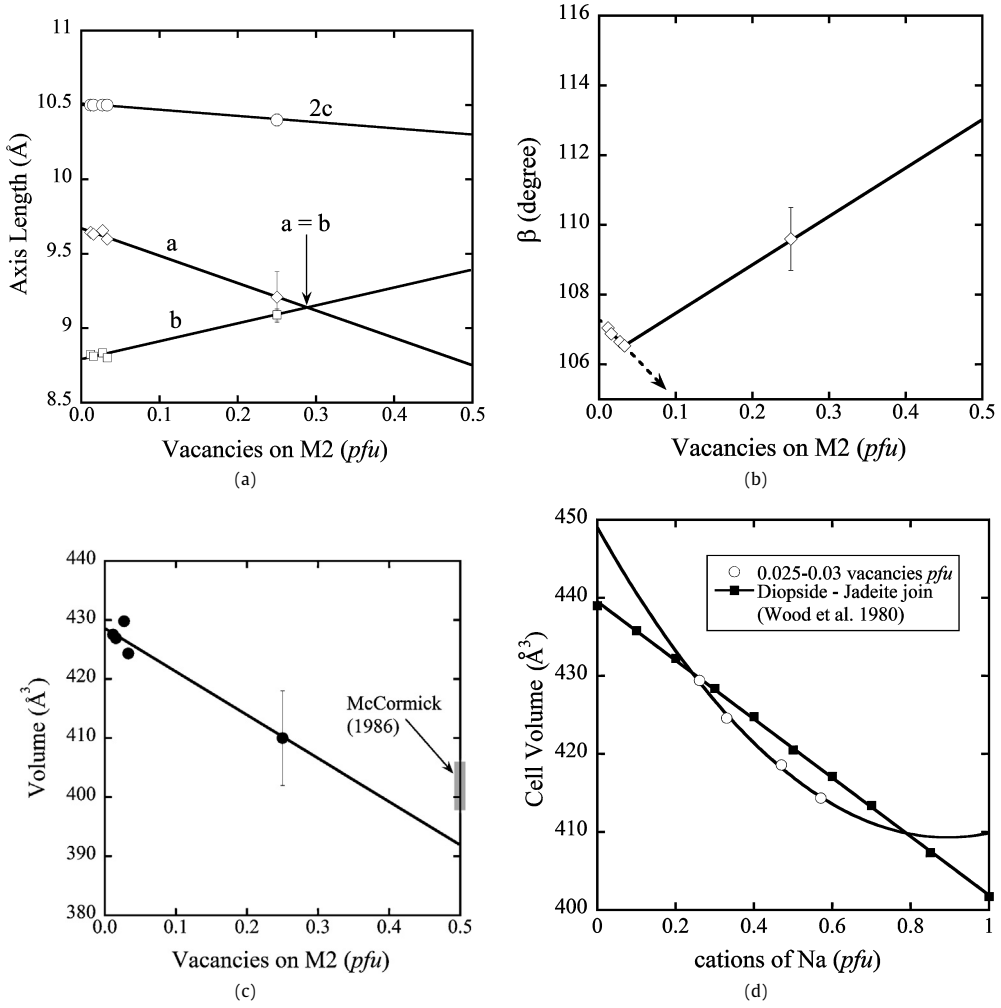

Fig. 4. Cell parameters for type tissintite (Ca# = 59) and $C2/c$ clinopyroxenes from the literature with Ca# of 54–64. The literature data are taken from McCormick (1986), Oberti and Caporuscio (1991), and Nestola et al. (2007) where the vacancy concentration was determined by structure analysis. Lines are unweighted regressions. (a) Cell parameters a, b, and 2 times c (for visual clarity) as a function of vacancy concentration. (b) Unique angle β as a function of vacancy concentration. (c) Cell volume as a function of vacancy concentration. The dashed lines are unweighted regression through the data and pertain to a Ca# of 54–64. In Fig. 3a, the vacancy concentration where a- and b-axes assume equal value is indicated. This may mark the point at which a spontaneous elastic instability of the defective pyroxene structure is induced. (d) Cell volume as a function of Na for clinopyroxenes with 0.025–0.30 vacancies *pfu*. Also shown are cell volumes for clinopyroxenes along the jadeite–diopside join (Wood et al., 1980).

Table 3
Symmetry modes for group–subgroup pair $P\bar{3}1c \rightarrow C2/c$. The index of this group–subgroup pair is 3 and the transformation matrix is b, -2a-b, c (read by columns).

(a) Symmetry modes summary (primary condensing modes in bold)		(b) Splitting of Wyckoff positions		
		No	Wyckoff position(s)	
WP	Modes		Group	Subgroup
12i	$\Gamma_1^+(3)\boldsymbol{\Gamma_3^+(6)}$	1	12i	8f 8f 8f
6h	$\Gamma_1^+(1)\boldsymbol{\Gamma_3^+(3)}$	2	6h	8f 4e
2c	$\boldsymbol{\Gamma_3^+(1)}$	3	2c	4e
2a	$\boldsymbol{\Gamma_3^+(1)}$	4	2a	4e

the Ca-Eskola component for a Ca# of 100. Clinopyroxenes have compositions plotting on or above this curve. A survey of experimental data from the literature encompassing simple to complex natural systems (references given in the caption to Fig. 5) yields a broad range of vacancy concentrations, depending on bulk composition, temperature, and pressure, but nearly all lie above the limiting vacancy curve. We interpret values beyond the hypothetical limit (two analyses from Massone and Fockenberg, 2012) to be analytical artifacts and probably within analytical error of being consistent with the vacancy limit. Note also that the limiting curve shown in Fig. 5 refers to full occupancy of M1 by trivalent cations; if the M1 site contains divalent cations, as it frequently does in high-pressure pyroxenes, then additional monovalent cations on M2 are required for charge balance, which further reduces the number of potentially available vacancies on the M2 site.

In Fig. 5, tissintite compositions plot close to the plagioclase join, well above the vacancy limit curve but with higher vacancy concentrations than observed in phase-equilibria studies (gray region in Fig. 5). Compositions of tissintites (Fig. 5) showing wormy intergrowths (e.g., Fig. 1) overlap those of rimming textural types (e.g., Fig. 2), suggesting that differences in composition are not at the root of the different textures. It seems likely that the basic formation mechanism for the two textural types is the same, and we, therefore, discuss their origin together.

We take three fundamental observations from the above descriptions: 1) tissintite forms from a plagioclase composition material (i.e., bulk compositions in the system of greatest interest lie along the anorthite–albite join); 2) it has a near-feldspar equivalent composition; and 3) there are no additional crystalline phases. In particular, no silica polymorph, garnet, corundum, aluminosilicate (e.g., kyanite), CAS phase, or hollandite-structured phase like lin-

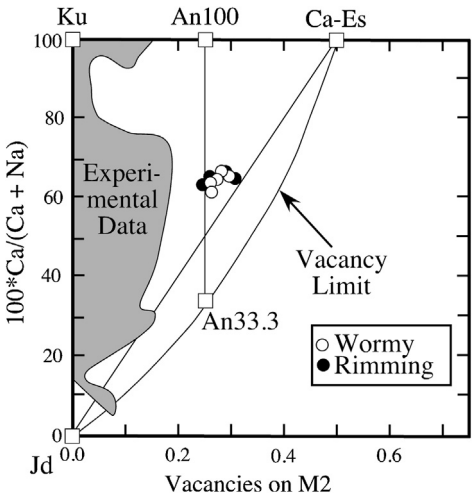

Fig. 5. Ca#, molar Ca/(Ca + Na), expressed as percent, in tissintite, as a function of the concentration of vacancies on the M2 site sorted by textural occurrence. Compositions of clinopyroxenes are restricted to the portion of the diagram on or above the curve labeled "Vacancy Limit," which defines the locus of points for which the M1 site is fully occupied with 3+ cations and the tetrahedral site by 4+ cations. Compositions for Ca–Na plagioclase defined in terms of a clinopyroxene formula unit, plot along a vertical line at an M2 vacancy concentration of 0.25; this line extends from end-member anorthite (Ca# of 100), labeled An100, to a Ca# of 33.3, below which clinopyroxene formulas based on M2 vacancies cannot be constructed from plagioclase. Compositions for jadeite (Jd), kushiroite (Ku), and the Ca-Eskola component (Ca-Es) are also shown. The gray field encloses data from equilibration and synthesis experiments of Wood and Henderson (1978), Gasparik (1984, 1985, 1986), Irifune et al. (1986), Ono and Yasuda (1996), Pertermann and Hirschmann (2002), Okamoto and Maruyama (2004), Zhao et al. (2011), Ishii et al. (2012), Massone and Fockenberg (2012), and Knapp et al. (2013).

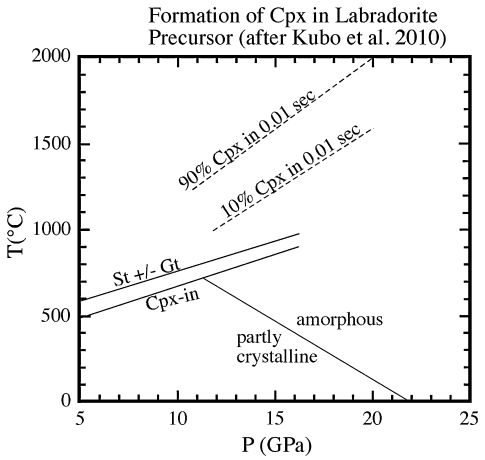

Fig. 6. Evolution of plagioclase (An58) during rapid heating and pressurization, modified after and combining elements of two figures in Kubo et al. (2010). The solid lines refer to experiments in which powdered natural labradorite was cold pressed and then heated (rate not stated). Amorphization versus X-ray diffraction occurs rapidly, within a second. If heated sufficiently, clinopyroxene (Cpx) nucleates and grows but with further heating, stishovite (St) ± garnet (Gt) grow and replace the clinopyroxene. Dashed lines are calculated amounts of clinopyroxene crystallized in 0.01 s after an instantaneous elevation of pressure and temperature, from ambient (e.g., after a shock event). Although presented quantitatively, this figure is best thought of as schematic. Fig. 6 is not a phase diagram and the appearance temperatures for clinopyroxene indicated on the figure are a measure of time at P and T, not a representation of stable phase fields. Kubo et al. (2010) determined volume fractions of clinopyroxene at constant pressure and temperature as a function of time; fit their data to an Avrami equation; and extrapolated the resulting kinetic parameters to the short-time scales of a shock event in order to calculate degrees of conversion of amorphous plagioclase composition material into clinopyroxene. Even on a relatively-short time scale, considerable crystallization of clinopyroxene is possible at relatively low temperatures (dashed lines in Fig. 6).

gunite is observed coexisting with tissintite. Phase equilibria for plagioclases of intermediate composition have not been studied in detail at high pressures and temperatures, so we first consider expectations based on the end-members albite and anorthite and then experiments conducted on bulk compositions off the plagioclase join. Finally, we evaluate constraints imposed by crystal growth theory and the subsolidus experiments of Kubo et al. (2010) on albite (An2) and labradorite (An58).

Above ~3 GPa, albite breaks down to form jadeite (i.e., a low-vacancy clinopyroxene) plus quartz or a silica-rich liquid. The jadeite is unstable relative to wadeite-structured $Na_2AlSi_2O_9$ plus stishovite or to a $CaFe_2SiO_4$-structured $NaAlSiO_4$ plus stishovite lingunite, the hollandite-structured form of $NaAlSi_3O_8$ above ~17 GPa (e.g., Liu, 1978; Presnall, 1995; Tutti et al., 2000; Tutti, 2007). Thus, based solely on the phase diagram for albite, a plausible origin for tissintite would be as a stable liquidus phase crystallizing from a plagioclase composition liquid; this would occur at shock pressures within the liquidus phase field of clinopyroxene (<~17 GPa for an albite bulk composition) with rapid quenching to prevent nucleation and growth of other phases. In this scenario, melting occurred in plagioclase enclaves within shock-melt pockets and those portions of large maskelynites closest to shock-melt pockets, as proposed by El Goresy and coworkers (Chen and El Goresy, 2000; El Goresy et al., 2013a); the tissintite crystallized as the liquidus phase from these melts. Portions of maskelynites further than ~25 μm from a melt pocket either didn't melt or were not heated sufficiently to allow for crystallization of tissintite. Although this mode of origin is attractive in its simplicity, caution must be exercised in extrapolating expectations based on albite all the way to the ~An65 relevant to tissintite; but, even if one were to do so, it provides no basis for asserting that tissintite, rather than a low-vacancy clinopyroxene is the stable liquidus phase. Clinopyroxene is not stable at all for an anorthite bulk composition; instead, anorthite at low pressures and temperatures forms a melt of anorthite composition and various phase assemblages involving two or more phases; these include corundum, grossular, kyanite, stishovite, $CaSiO_3$ perovskite, and the CAS phase, $CaAl_4Si_2O_{11}$ (Presnall, 1995; Liu et al., 2012). Based solely on data for the anorthite bulk composition, tissintite is not a stable phase – i.e., there must be an upper limit to the Ca# of tissintite on the plagioclase join. Moreover, based on a fairly large collection of experiments described in the literature (sources given in the caption to Fig. 5), clinopyroxene coexisting with another crystalline phase will have a much lower vacancy concentration than tissintite. If this holds generally, then tissintite is always metastable, outside a primary phase field for clinopyroxene, relative to a phase assemblage; this would contain either no clinopyroxene or one that contains a low-vacancy clinopyroxene (i.e., not tissintite). Thus, one key to the presence of tissintite appears to be the absence of co-crystallizing phases.

Kubo et al. (2010) investigated the amorphization of and crystallization in a natural labradorite (An58), which is quite close to that of the type material (Ca# = 59), through *in situ* multi-anvil experiments at 8–26 GPa and relatively low subsolidus temperatures (<~1000 °C). In one set of experiments, Kubo et al. (2010) cold-pressurized the plagioclase and then heated it (see solid lines in Fig. 6) with the key result that clinopyroxene (tissintite?) was the first crystalline phase to nucleate; but other phases have faster growth rates. The experiments of Kubo et al. refer to subsolidus conditions, but the same nucleation advantages likely hold for crystallization from a melt (i.e., a tissintite crystal nucleates in a melt of essentially the same composition, so it may thereby require fewer perturbations to initiate nucleation and growth than other phases). Given the results of Kubo et al., there are three basic possibilities for the formation of tissintite: (1) crystallization from a melt as the liquidus phase; (2) subliquidus crystallization from a melt due to enhanced nucleation rates; (3) crystallization

from amorphous glassy material. We can reject the third option because the long time scale for subsolidus crystallization would require a very large shock, which is inconsistent with several lines of evidence suggesting that Tissint formed in a relatively small shock event (e.g., Walton et al., 2014). The first two options are currently indistinguishable as available experimental data do not establish whether or not tissintite is the liquidus phase. We can, however, place some constraints on the nature of tissintite crystallization. If plagioclase completely melted, as championed by Chen and El Goresy (2000) and El Goresy et al. (2013a), for shergottites in general and El Goresy et al. (2013b) for Tissint, in particular, then quenching must have been sufficiently fast that no phase that could provide an exchange mechanism for vacancies (e.g., stishovite) crystallized during cooling. Moreover, tissintite is only present in maskelynite enclosed by or within ~25 μm of a melt pocket, either indicating that only those portions of the maskelynite melted, or if all were melted, only those regions closest to a melt pocket were heated long enough to support the growth of tissintite. Otherwise, tissintite would be ubiquitous in maskelynite, independent of distance from melt pockets, instead of being so spatially restricted.

Observed tissintites in Tissint show a limited range in Ca#s (58–69) and it is important to establish whether this reflects real limits on composition or simply the local limitation of Tissint's plagioclase compositions and shock conditions. As noted above, there are stoichiometry and phase equilibria constraints that limit Ca# in tissintite on the $NaAlSi_3O_8$–$CaAl_2Si_2O_8$ join to $33 < Ca\# < 100$. There are also likely to be kinetic constraints. Muncill and Lasaga (1987) developed a general equation for the growth of binary plagioclase during crystallization from a liquid and the ratio of two such equations can be adapted to a pair of tissintites with modestly differing Ca#s (e.g., 60 vs. 50). Provided growth mechanisms are the same, the relative growth rates depend weakly on differences in the equilibrium constant K_e for Na–Ca exchange between tissintite and melt [for $K_e \sim 1$, as expected based on compositions of coexisting maskelynite and tissintite (see Table 1)] and enthalpies of melting (provided those for Na- and Ca-endmembers are within the range shown by other Na- and Ca-aluminosilicates (e.g., Richet and Bottinga, 1986). The relative growth rate is, however, sensitive to ΔT, the difference between liquidus and crystallization temperatures, which acts to increase growth rate with decreasing temperature due to the increasing deviation from equilibrium, and fluidity, the inverse of the viscosity, which acts to decrease growth rate with decreasing temperature. Viscosities for melt compositions along the anorthite–albite binary are known at 1 atm. (e.g., Hummel and Arndt, 1985; Muncill and Lasaga, 1987). The pressure dependence is less well constrained but both $CaAl_2Si_2O_8$ and $NaAlSi_3O_8$ show minima as a function of pressure at ~5 GPa and similar relative changes in viscosity (e.g., Funakoshi et al., 2002; Del Gaudio and Behrens, 2009; Karki et al., 2011). Overall, we therefore expect the viscosity to decrease with decreasing temperature at constant composition and to decrease with increasing Ca# at constant temperature and pressure. According to the clinopyroxene-melt model of Putirka et al. (2003), decreasing the Ca# from 60 to 50 lowers the liquidus temperature by ~50°. If the equilibrium temperatures for tissintites are also higher for more calcic compositions, then, at any given temperature during growth, the more calcic tissintite will grow faster. This conclusion dovetails with the observation of Kubo et al. (2010) that clinopyroxene and subsequent phases crystallize much faster in amorphous labradorite than in amorphous albite, at the same pressures and temperatures. If true generally, then crystallizing tissintite from a plagioclase more sodic than observed in Tissint (Ca# of 58–69) requires more time at high temperatures (i.e., a shock intensity greater than observed for Tissint or a propensity to form larger melt pools that cooled more slowly than in Tissint). However, more time at elevated pressures and temperatures potentially allows additional phases to appear that would destroy the tissintite. Therefore, once formed, a calcic tissintite in a small shock is more likely to survive than a sodic tissintite in a larger shock. This makes tissintite a phase of immense potential for constraining shock conditions. Tissintite of a given composition can only form over a small range of P–T–t. With experimental calibration, tissintite may therefore provide explicit statements of conditions during the shock event and its absence can impose robust lower limits on the shock intensity. We note that such constraints refer to plagioclase precursor compositions at or near the interface with a shock melt pocket or vein; they do not speak to the entire range of maskelynite compositions or to melt compositions off the plagioclase join. In martian meteorites, the Ca# in maskelynite ranges from ~20 to ~70 (e.g., Fritz et al., 2005; Papike et al., 2009) but the more calcic compositions within a given meteorite are usually located in the cores of maskelynites where they would probably not have been heated sufficiently to crystallize tissintite. Tissintite may occur unnoticed in a variety of shergottites. However, the most promising candidates for tissintite in martian meteorites are the depleted olivine-phyric shergottites (NWA 4925, NWA 5789, NWA 5990, and Tissint, of which we have only investigated Tissint). In these meteorites, most of the maskelynite in contact with shock melt pockets is more calcic than An60, and shock intensities may have been similar.

As noted above in discussing Fig. 5, tissintite cannot form in sodic-plagioclase precursors (<An33). Therefore, based on observed plagioclase compositions (Brearley and Jones, 1998; Mittlefeldt et al., 1998), tissintite is unlikely to be found in highly equilibrated ordinary chondrites, enstatite achondrites, lodranites, or acapulcoites, even were they to be heavily shocked, although low-vacancy jadeites could form, as is observed in ordinary chondrites (Miyahara et al., 2013 and references therein). Similarly, plagioclase in many terrestrial impact sites is too sodic to produce tissintite [e.g., the clinopyroxenes in ~An20 maskelynites from the Ries crater (James, 1969) are jadeites and not tissintites]. The maximum Ca# for a plagioclase that can potentially yield tissintite is unknown beyond being <100 but feldspars in Ca-, Al-rich inclusions from carbonaceous chondrites are probably too calcic [typically, An99–100; Brearley and Jones, 1998]. There are, however, many potential target rocks with plagioclase compositions more appropriate for the formation of tissintite. The country rock at the Lonar crater in India is dominantly composed of basalts containing labradorite phenocrysts (Kieffer et al., 1976) and plagioclase is ~An55 at the terrestrial Manicouagan impact site in Quebec (White, 1993). Calcic igneous plagioclase with An60–An85 is observed in ferromagnesian and Al-rich chondrules from carbonaceous, enstatite, R, and unequilibrated and moderately equilibrated ordinary chondrites (Brearley and Jones, 1998). Most of these meteorites are only lightly shocked (or annealed after heavy shocks) but, where heavily shocked, tissintite is a possibility. Plagioclase in lunar rocks is generally quite calcic, and some lunar meteorites are heavily shocked (Papike et al., 1998; Lin et al., 2012), so tissintite may well occur in them.

5. Summary

Tissintite, $(Ca, Na, \square)AlSi_2O_6$, is an extraordinarily vacancy-rich, dense $C2/c$ clinopyroxene with a plagioclase equivalent composition (An58–An69) that formed in the Tissint martian meteorite during a shock event that was severe enough to allow its nucleation and growth from plagioclase precursors in or near shock-melt pockets; but, not so severe that other phases, which would have destroyed the tissintite, could nucleate and grow. Tissintite is most likely to be found in martian, terrestrial, and lunar rocks with calcic plagioclase shocked intensely enough to produce melt pockets

and/or veins. More sodic tissintites than observed in Tissint may well be stable along the $NaAlSi_3O_8$–$CaAl_2Si_2O_8$ binary but these would likely require greater shock intensities than for Tissint because of slower growth rates. Tissintite cannot be constructed from a plagioclase more sodic than An33, so it is unlikely to be observed in most ordinary chondrites.

The intersection of the *a*- and *b*- axis lengths for $C2/c$ clinopyroxenes at a vacancy concentration of ∼0.3 *pfu*, for Ca# ∼60, suggests a spontaneous elastic instability leading to a disordered trigonal structure and a corresponding limit to vacancy concentrations that is quite close to the maximum observed in meteoritic tissintite. This mechanism may be important in defining vacancy concentration limits for tissintites with higher or lower Ca#s. With experimental calibration, tissintite may provide explicit statements of conditions during the shock event and its absence can impose robust lower limits on the shock intensity.

Acknowledgements

SEM, EBSD and EPMA analyses were carried out at the Caltech GPS Division Analytical Facility, which is supported, in part, by NSF Grants EAR-0318518 and DMR-0080065. Synchrotron diffraction was carried out at the 13-IDD beamline of the Advanced Photon Source and the 12.2.2 beamline of the Advanced Light Source. Use of the Advanced Photon Source, an Office of Science User Facility operated for the U.S. Department of Energy (DOE) Office of Science by Argonne National Laboratory, was supported by the U.S. DOE under Contract No. DE-AC02-06CH11357. The Advanced Light Source is supported by the Director, Office of Science, Office of Basic Energy Sciences, of the U.S. Department of Energy under Contract No. DE-AC02-05CH11231. OT acknowledges the support from DOE Cooperative Agreement #DE-NA0001982. GRR acknowledges NSF EAR grant 322082. YL acknowledges support from Jet Propulsion Laboratory, which is managed by California Institute of Technology under a contract with NASA, and NASA grant NNN13D465T. LAT and JRB acknowledge NASA Cosmochemistry grants NNX11AG58G and NNX12AH63G, respectively. PD gratefully acknowledges support from NSF grants EAR 1344942 and 1440005. Formal reviews by A. El Goresy and an anonymous reviewer and additional comments by T. Kubo all led to significant improvements.

Appendix A. Supplementary material

Supplementary material related to this article can be found online at http://dx.doi.org/10.1016/j.epsl.2015.03.057.

References

Ahrens, T.J., Asimow, P.D., Mosenfelder, J.L., 2009. Advances in shock compression of mantle minerals and implications. AIP Conf. Proc. 1195, 859. http://dx.doi.org/10.1063/1.3295278.

Akaogi, M., 2007. Phase transitions of minerals in the transition zone and upper part of the lower mantle. In: Ohtani, E. (Ed.), Advances in High-Pressure Mineralogy. In: Spec. Pap., Geol. Soc. Am., vol. 421, pp. 1–13.

Aoudjehane, H.C., Avice, G., Barrat, J.-A., Boudouma, O., Chen, G., Duke, M.J.M., Franchi, I.A., Gattacceca, J., Grady, M.M., Greenwood, R.C., Herd, C.D.K., Hewins, R., Jambon, A., Marty, B., Rochette, P., Smith, C.L., Sautter, V., Verchovsky, A., Weber, P., Zanda, B., 2012. Tissint Martian meteorite: a fresh look at the interior, surface, and atmosphere of Mars. Science 338, 785–788.

Armstrong, J.T., 1995. CITZAF: a package of correction programs for the quantitative electron microbeam X-ray analysis of thick polished materials, thin films, and particles. Microbeam Anal. 4, 177–200.

Baziotis, I.P., Liu, Y., DeCarli, P.S., Melosh, H.J., McSween, H.Y., Bodnar, R.J., Taylor, L.A., 2013. The Tissint Martian meteorite as evidence for the largest impact excavation. Nat. Commun. 4, 1404. http://dx.doi.org/10.1038/ncomms2414.

Brearley, A.J., Jones, R.H., 1998. Chondritic meteorites. Rev. Miner. 36, 3-1–3-398.

Chen, M., El Goresy, A., 2000. The nature of maskelynite in shocked meteorites: not diaplectic glass but a glass quenched from shock-induced dense melt at high pressures. Earth Planet. Sci. Lett. 179, 489–502.

Del Gaudio, P., Behrens, H., 2009. An experimental study on the pressure dependence of viscosity in silicate melts. J. Chem. Phys. 131, 044504.

Dera, P., Zhuravlev, K., Prakapenka, V., Rivers, M.L., Finkelstein, G.J., Grubor-Urosevic, O., Tschauner, O., Clark, S.M., Downs, R.T., 2013. High pressure single-crystal micro X-ray diffraction analysis with GSE_ADA/RSV software. High Press. Res. 33, 466–484.

El Goresy, A., Gillet, Ph., Miyahara, M., Ohtani, E., Ozawa, S., Beck, P., Montagnac, G., 2013a. Shock-induced deformation of shergottites: shock-pressures and perturbations of magmatic ages on Mars. Geochim. Cosmochim. Acta 101, 233–262.

El Goresy, A., Gillet, Ph., Miyahara, M., Ohtani, E., Ozawa, S., Lin, Y., Feng, L., Escerig, S., 2013b. Multiple shock events and diamond formation on Mars. In: 44th Lunar Planet. Sci. Conf. 1037.pdf.

Fritz, J., Greshake, A., Stöffler, D., 2005. Micro-Raman spectroscopy of plagioclase and maskelynite in Martian meteorites: evidence of progressive shock metamorphism. Antarct. Meteor. Res. 18, 96–116.

Funakoshi, K.-i., Suzuki, A., Terasaki, H., 2002. *In situ* viscosity measurements of albite melt under high pressure. J. Phys. Condens. Matter 14, 11343–11347.

Gasparik, T., 1984. Experimentally determined stability of clinopyroxene + garnet + corundum in the system CaO–MgO–Al_2O_3–SiO_2. Am. Mineral. 69, 1025–1035.

Gasparik, T., 1985. Experimental study of subsolidus phase relations and mixing properties of pyroxene and plagioclase in the system Na_2O–CaO–Al_2O_3–SiO_2. Contrib. Mineral. Petrol. 89, 346–357.

Gasparik, T., 1986. Experimental study of subsolidus phase relations and mixing properties of clinopyroxene in the silica-saturated system CaO–MgO–Al_2O_3–SiO_2. Am. Mineral. 71, 686–693.

Hammersley, A.P., Svensson, S.O., Hanfland, M., Fitch, A.N., Hausermann, D., 1996. Two-dimensional detector software: from real detector to idealised image or two-theta scan. High Press. Res. 14, 235–248.

Herd, C.D.K., Duke, M.J.M., Bryden, C.D., Pearson, D.G., 2013. Tissint among the shergottites: parental melt composition, redox state, La/Yb and V/Sc. In: 44th Lunar Planet. Sci. Conf. 2683.pdf.

Hirose, K., Labrosse, S., Hernlund, J., 2014. Composition and state of the Earth's core. Annu. Rev. Earth Planet. Sci. 41, 657–691.

Hummel, W., Arndt, J., 1985. Variation of viscosity with temperature and composition in the plagioclase system. Contrib. Mineral. Petrol. 90, 83–92.

Irifune, T., Sekine, T., Ringwood, A.E., Hibberson, W.O., 1986. The eclogite–garnetite transformation at high pressure and some geophysical implications. Earth Planet. Sci. Lett. 77, 245–256.

Ishii, T., Kojitani, H., Akaogi, M., 2012. High-pressure phase transitions and subduction behavior of continental crust at pressure–temperature conditions up to the upper part of the lower mantle. Earth Planet. Sci. Lett. 357–358, 31–41.

James, O.B., 1969. Jadeite: shock-induced formation from oligoclase, Ries crater, Germany. Science 165, 1005–1008.

Johnston, C.L., Gunter, M.E., Knowles, C.R., 1991. Sunstone labradorite from the Ponderosa Mine, Oregon. Gems. Gemol. 27, 220–233.

Karki, B.B., Bohara, B., Stixrude, L., 2011. First-principles study of diffusion and viscosity of anorthite ($CaAl_2Si_2O_8$) liquid at high pressure. Am. Mineral. 96, 744–751.

Katayama, I., Parkinson, C.D., Okamoto, K., Nakajima, Y., Maruyama, S., 2000. Supersilicic clinopyroxene and silica exsolution in UHPM eclogite and pelitic gneiss from the Kokchetav massif, Kazakhstan. Am. Mineral. 85, 1368–1374.

Kieffer, S.W., Schaal, R.B., Gibbons, R., Hörz, F., Milton, D.J., Dube, A., 1976. Shocked basalt from Lonar impact crater, India, and experimental analogues. In: Proc. 7th Lunar Planet. Sci. Conf., pp. 1391–1412.

Kimura, M., Mikouchi, T., Suzuki, A., Miyahara, M., Ohtani, E., El Goresy, A., 2009. Kushiroite, $CaAlAlSiO_6$: a new mineral of the pyroxene group from the ALH 85085 CH chondrite, and its genetic significance in refractory inclusions. Am. Mineral. 94, 1479–1482.

Kinomura, N., Kume, S., Koizumi, M., 1975. Stability of $K_2Si_4O_9$ with wadeite type structure. In: Proc. 4th Int. Conf. High Pressure Sci. Tech., pp. 211–214.

Knapp, N., Woodland, A.B., Klimm, K., 2013. Experimental constraints in the CMAS system on the Ca-Eskola content of eclogitic clinopyroxene. Eur. J. Mineral. 25, 579–596.

Konzett, J., Frost, D.J., Proyer, A., Ulmer, P., 2008. The Ca-Eskola component in eclogitic clinopyroxene as a function of pressure, temperature and bulk composition: an experimental study to 15 GPa with possible implications for the formation of oriented SiO_2-inclusions in omphacite. Contrib. Mineral. Petrol. 155, 215–228.

Kubo, T., Kimura, M., Kato, T., Nishi, M., Tominaga, A., Kikegawa, T., Funakoshi, K., 2010. Plagioclase breakdown as an indicator for shock conditions of meteorites. Nat. Geosci. 3, 41–45.

Kuchka, C.R., Walton, E.L., Herd, C.D.K., 2013. Shock melt features in Los Angeles and Tissint: a comparison. In: 44th Lunar Planet. Sci. Conf. 3043.pdf.

Lin, Y., Shen, W., Liu, Y., Xu, L., Hofmann, B.A., Mao, Q., Tang, G.Q., Wu, F., Li, X.H., 2012. Very high-K KREEP-rich clasts in the impact melt breccia of the lunar meteorite SaU 169: new constraints on the last residue of the Lunar Magma Ocean. Geochim. Cosmochim. Acta 85, 19–40.

Litvin, Y., Spivak, A., Solopova, N., Dubrovinsky, L., 2014. On origin of lower-mantle diamonds and their primary inclusions. Phys. Earth Planet. Inter. 228, 176–185.

Liu, L.-G., 1978. High-pressure phase transformations of albite, jadeite and nepheline. Earth Planet. Sci. Lett. 37, 438–444.

Liu, X., Ohfuji, H., Nishiyama, N., He, Q., Sanehira, T., Irifune, T., 2012. High-P behavior of anorthite composition and some phase relations of the $CaO–Al_2O_3–SiO_2$ system to the lower mantle of the Earth and their geophysical implications. J. Geophys. Res. 117, B09205. http://dx.doi.org/10.1029/2012JB009290.

Ma, C., Rossman, G.R., 2008. Barioperovskite, $BaTiO_3$, a new mineral from the Benitoite Mine, California. Am. Mineral. 93, 154–157.

Ma, C., Rossman, G.R., 2009. Tistarite, Ti_2O_3, a new refractory mineral from the Allende meteorite. Am. Mineral. 94, 841–844.

Ma, C., Simon, S.B., Rossman, G.R., Grossman, L., 2009. Calcium Tschermak's pyroxene, $CaAlAlSiO_6$ from the Allende and Murray meteorites: EBSD and micro-Raman characterizations. Am. Mineral. 94, 1483–1486.

Ma, C., Liu, Y., Tschauner, O., 2013a. Tissintite, IMA 2013-027. CNMNC Newsletter No. 16, August 2013, p. 2707, Mineral. Mag. 77, 2695–2709.

Ma, C., Tschauner, O., Liu, Y., Sinogeikin, S., 2013b. Ahrensite, IMA 2013-028. CNMNC Newsletter No. 16, August 2013, p. 2707, Mineral. Mag. 77, 2695–2709.

Ma, C., Tschauner, O., Liu, Y., Beckett, J.R., Rossman, G.R., Zuravlev, K., Prakapenka, V., Dera, P., Sinogeikin, S., Smith, J., Taylor, L.A., 2014. Discovery of ahrensite γ-Fe_2SiO_4 and tissintite $(Ca,Na,\square)AlSi_2O_6$: two new high pressure minerals from the Tissint Martian meteorite. In: 45th Lunar Planet. Sci. Conf. 1222.pdf.

Massone, H.-J., Fockenberg, T., 2012. Melting of metasedimentary rocks at ultrahigh pressure—insights from experiments and thermodynamic calculations. Lithosphere 4, 269–285.

McCormick, T.C., 1986. Crystal-chemical aspects of nonstoichiometric pyroxenes. Am. Mineral. 71, 1434–1440.

Mittlefeldt, D.W., McCoy, T.J., Goodrich, C.A., Kracher, A., 1998. Non-chondritic meteorites from asteroidal bodies. Rev. Miner. 36, 4-1–4-195.

Miyahara, M., Ozawa, S., Ohtani, E., Kimura, M., Kubo, T., Sakai, T., Nagase, T., Nishijima, M., Hirao, N., 2013. Jadeite formation in shocked ordinary chondrites. Earth Planet. Sci. Lett. 373, 102–108.

Muncill, G.E., Lasaga, A.C., 1987. Crystal-growth kinetics of plagioclase in igneous systems: one-atmosphere experiments and application of a simplified growth model. Am. Mineral. 72, 299–311.

Nestola, F., Longo, M., McCammon, C., Boffa Ballaran, T., 2007. Crystal-structure refinement of Na-bearing clinopyroxenes from mantle-derived eclogite xenoliths. Am. Mineral. 92, 1242–1245.

Oberti, R., Caporuscio, F.A., 1991. Crystal chemistry of clinopyroxenes from mantle eclogites: a study of the key role of the M2 site population by means of crystal-structure refinement. Am. Mineral. 76, 1141–1152.

Ohtani, E., Kimura, Y., Kimura, M., Takata, T., Kondo, T., Kubo, T., 2004. Formation of high-pressure minerals in shocked L6 chondrite Yamato 791384: constraints on shock conditions and parent body size. Earth Planet. Sci. Lett. 227, 505–515.

Okamoto, K., Maruyama, S., 2004. The eclogite–garnetite transformation in the MORB + H_2O system. Phys. Earth Planet. Inter. 146, 283–296.

Ono, S., Yasuda, A., 1996. Compositional change of majoritic garnet in a MORB composition from 7 to 17 GPa and 1400 to 1600 °C. Phys. Earth Planet. Inter. 96, 171–179.

Papike, J.J., Ryder, G., Shearer, C., 1998. Lunar samples. Rev. Miner. 36, 5-1–5-234.

Papike, J.J., Karner, J.M., Shearer, C.K., Burger, P.V., 2009. Silicate mineralogy of martian meteorites. Geochim. Cosmochim. Acta 73, 7443–7485.

Pertermann, M., Hirschmann, M.M., 2002. Trace-element partitioning between vacancy-rich eclogitic clinopyroxene and silicate melt. Am. Mineral. 87, 1365–1376.

Prencipe, M., 2012. Simulation of vibrational spectra of crystals by ab initio calculations: an invaluable aid in the assignment and interpretation of the Raman signals. The case of jadeite ($NaAlSi_2O_6$). J. Raman Spectrosc. 43, 1567–1569.

Presnall, D.C., 1995. Phase diagrams of Earth-forming minerals. In: Ahrens, T.J. (Ed.), Handbook of Physical Constants, Mineral Physics and Crystallography. Am. Geophys. Union, Washington, DC, pp. 248–268.

Putirka, K.D., Mikaelian, H., Ryerson, F., Shaw, H., 2003. New clinopyroxene-liquid thermobarometers for mafic, evolved, and volatile-bearing lava compositions, with applications to lavas from Tibet and the Snake River Plain, Idaho. Am. Mineral. 88, 1542–1554.

Richet, P., Bottinga, Y., 1986. Thermochemical properties of glasses and liquids: a review. Rev. Geophys. 24, 1–25.

Sharp, T.G., DeCarli, P.S., 2006. Shock effects in meteorites. In: Lauretta, D.S., McSween, H.Y. (Eds.), Meteorites and the Early Solar System II. University of Arizona Press, Tucson, pp. 653–677.

Smyth, J.R., 1980. Cation vacancies and the crystal chemistry of breakdown reactions in kimberlitic omphacites. Am. Mineral. 65, 1185–1191.

Stixrude, L., Lithgow-Bertelloni, C., 2012. Geophysics of chemical heterogeneity in the mantle. Annu. Rev. Earth Planet. Sci. 40, 569–595.

Stöffler, D., Keil, K., Scott, E.R.D., 1991. Shock metamorphism of ordinary chondrites. Geochim. Cosmochim. Acta 55, 3845–3867.

Tutti, F., 2007. Formation of end-member $NaAlSi_3O_8$ hollandite-type structure (lingunite) in diamond anvil cell. Phys. Earth Planet. Inter. 161, 143–149.

Tutti, F., Dubrovinsky, L.S., Saxena, S.K., 2000. High pressure phase transformation of jadeite and stability of $NaAlSiO_4$ with calcium-ferrite type structure in the lower mantle conditions. Geophys. Res. Lett. 27, 2025–2028.

Udry, A., Balta, J.B., McSween, H.Y., 2013. CSD measurements on olivine grains in the Tissint meteorite. In: 44th Lunar Planet. Sci. Conf. 1266.pdf.

Von Dreele, R.B., 1997. Quantitative texture analysis by Rietveld refinement. J. Appl. Crystallogr. 30, 517–525.

Walton, E.L., Sharp, T.G., Hu, J., Filiberto, J., 2014. Heterogeneous mineral assemblages in martian meteorite Tissint as a result of a recent small impact event on Mars. Geochim. Cosmochim. Acta 140, 334–348.

White, J.C., 1993. Shock-induced amorphous textures in plagioclase, Manicouagan, Quebec, Canada. Contrib. Mineral. Petrol. 113, 524–532.

Wood, B.J., Henderson, C.M.B., 1978. Compositions and unit-cell parameters of synthetic non-stoichiometric tschermakitic clinopyroxenes. Am. Mineral. 63, 66–72.

Wood, B.J., Holland, T.J.B., Newton, R.C., Kleppa, O.J., 1980. Thermochemistry of jadeite–diopside pyroxenes. Geochim. Cosmochim. Acta 44, 1363–1371.

Yagi, A., Suzuki, T., Akaogi, M., 1994. High pressure transitions in the system $KAlSi_3O_8$–$NaAlSi_3O_8$. Phys. Chem. Miner. 21, 12–17.

Yang, H., Konzett, J., Frost, D.J., Downs, R.T., 2009. X-ray diffraction and Raman spectroscopic study of clinopyroxenes with six-coordinated Si in the $Na(Mg_{0.5}Si_{0.5})Si_2O_6$–$NaAlSi_2O_6$ system. Am. Mineral. 94, 942–949.

Zhao, S., Nee, P., Green, H.W., Dobrzhinetskaya, L.F., 2011. Ca-Eskola component in clinopyroxene: experimental studies at high pressures and high temperatures in multianvil apparatus. Earth Planet. Sci. Lett. 307, 517–524.